THE JOURNAL OF PHYSICAL CHEMISTRY C
Article
Cite This: J. Phys. Chem. C 2019, 123, 2792−2800
pubs.acs.org/JPCC

Enhancing Lithium Adsorption and Diffusion toward Extraordinary Lithium Storage Capability of Freestanding $Ti_3C_2T_x$ MXene

Haitao Zhang,[†,⊥] Xiaojun Xin,[§,⊥] Huan Liu,[∥] Haichao Huang,[†] Ningjun Chen,[†] Yanting Xie,[†] Weili Deng,[†] Chunsheng Guo,[*,†] and Weiqing Yang[*,†,‡]

[†]Key Laboratory of Advanced Technologies of Materials (Ministry of Education), School of Materials Science and Engineering and [‡]State Key Laboratory of Traction Power, Southwest Jiaotong University, Chengdu 610031, P. R. China

[§]Key laboratory of Magnetic levitation Technologies and Maglev Trains (Ministry of Education), Superconductivity and New Energy R&D Center, Southwest Jiaotong University, Mail Stop 165#, Chengdu 610031, P. R. China

[∥]State Key Laboratory of Silicon Materials, Department of Materials Science and Engineering, Zhejiang University, Hangzhou, Zhejiang 310027, P. R. China

Supporting Information

ABSTRACT: Chemical etching method shows potential for large-scale and low-cost processed MXenes but incorporates surface terminations such as F&OH that probably deteriorate the lithium storage characteristics. Herein, we propose that tailoring appropriate surface functionalization and the intrinsic electrical properties can dramatically enhance the lithium storage capability of $Ti_3C_2T_x$ (T stands for F, OH, and O) MXene materials. By carefully controlling the annealing process, the $Ti_3C_2T_x$ films possess fewer F&OH elements so that with higher conductivity, they are still freestanding and flexible. Density functional theory computations of the low-F&OH-containing $Ti_3C_2T_x$ show low-ion-diffusion barrier values of 0.34−0.43 eV and a significant increase of Li adsorption energy by 6−30 times compared to those of high-F&OH-containing $Ti_3C_2T_x$, suggesting high Li-ion storage and transfer capabilities can be achieved in low-F&OH-containing $Ti_3C_2T_x$ MXenes. Dramatically, the heteroatom-controlled $Ti_3C_2T_x$ MXene films show reversible capacities of 221 mAh g^{-1} for lithium-ion batteries at a current density of 0.1 C (1 C = 320 mAh g^{-1}), which is the highest up to now for pure Ti-based MXenes. These results demonstrate the importance of surface chemistry and electronic structure of MXene in the lithium storage capability, which provides valuable information on designing high-performance MXene-based materials for energy storage, optoelectronic, thermoelectric, and magnetic applications.

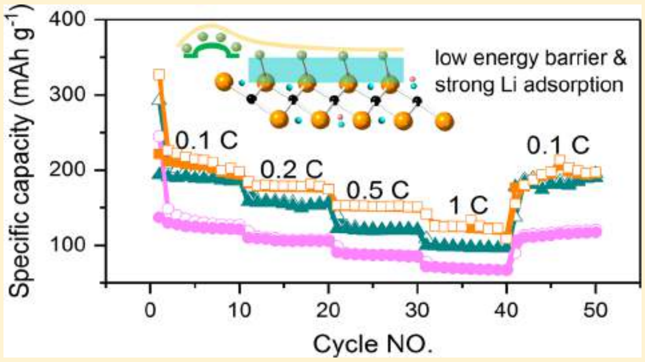

1. INTRODUCTION

Due to their high surface-bulk ratios, large interlayer spacing, and low diffusion barriers, two-dimensional (2D) materials have been predicted to provide high Li capacities and superior cycling rates as anodes.[1−5] Ti_3C_2 MXene, the first discovered and the most widely studied 2D MXene materials to date,[6] shows promise as anode material for Li-ion batteries (LIBs) because of its exceptional properties, including good electronic conductivity, fast Li diffusion, and high theoretical capacity.[7−9] The bare Ti_3C_2 monolayer exhibits a low barrier for Li diffusion and high Li storage capacity (up to $Ti_3C_2Li_2$ stoichiometry). Density functional theory (DFT) computations predicted that an isolated Li atom diffusion barrier on the Ti_3C_2 is only 0.07 eV,[10] which is much lower than that in other typical anode materials, like graphite (∼0.3 eV)[11] and lithium titanate (0.3−0.48 eV).[12] The high theoretical capacity and low Li diffusion barriers in monolayer MXenes indicate that these materials may, indeed, be suitable candidates for exploiting simultaneously high-energy and high-power LIBs that are especially essential for state-of-the-art LIBs. However, the unique Li storage properties of MXenes stop at theoretical predictions,[13−16] and experimental recognition has not been sufficiently made.

Generally, the Li storage and diffusion properties of MXenes can be modulated by physical and chemical treatments. MXenes are usually terminated by many heteroatoms like F, OH, and O due to the presence of HF and H_2O during solution-based preparing methods.[17−21] These heteroatoms usually cause decrease of Li content and the electrical conductivity, leading to lower Li storage capacities and diffusion rate. DFT computations implied that the theoretical Li storage capacity of Ti_3C_2 MXenes could be dramatically improved by the removal of F groups from the surfaces.[10] Experimentally, R.B. Rakhi et al. claimed that the super-

Received: November 20, 2018
Revised: December 28, 2018
Published: January 10, 2019

DOI: 10.1021/acs.jpcc.8b11255
J. Phys. Chem. C 2019, 123, 2792−2800

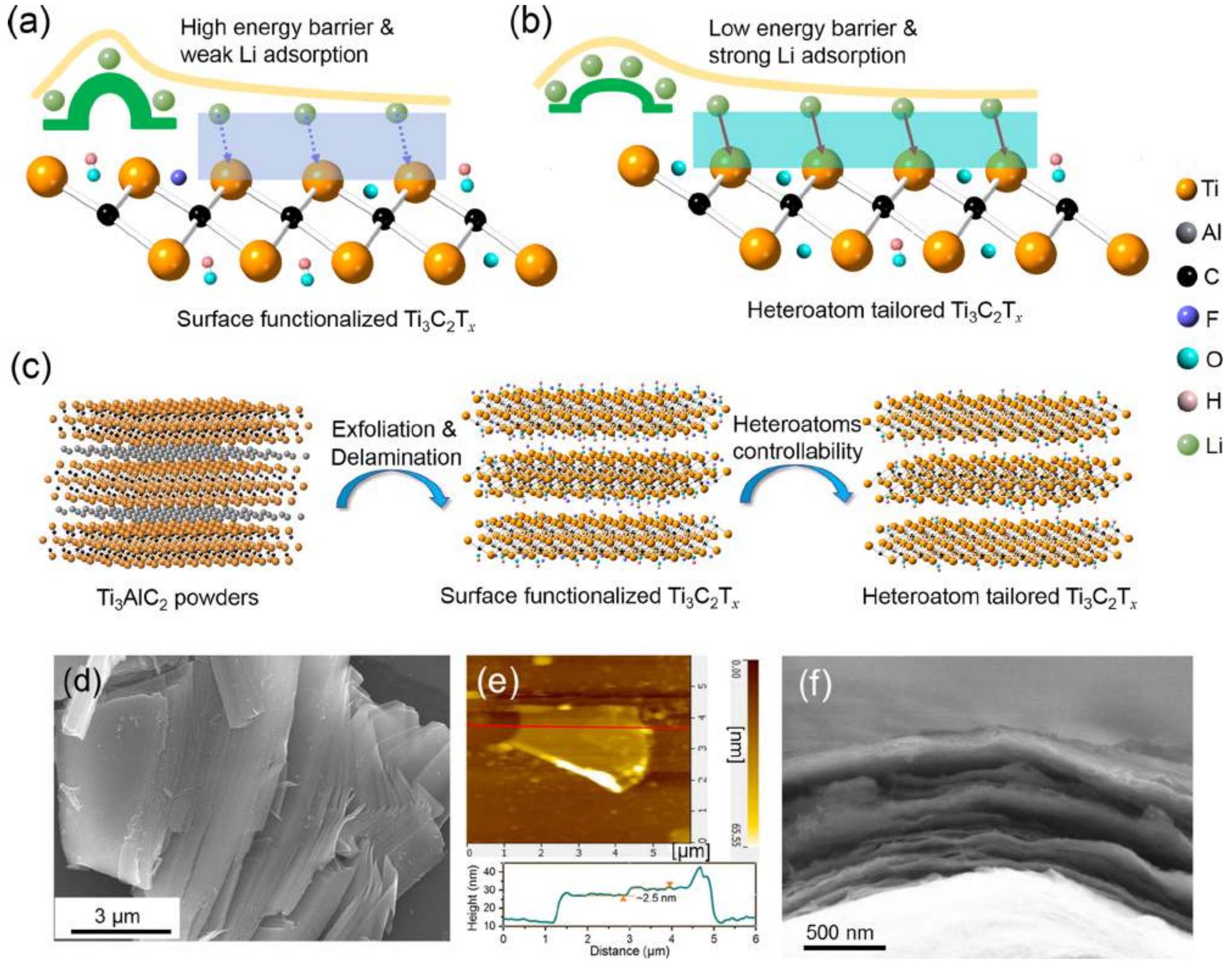

Figure 1. Designing high lithium-ion storage capability for $Ti_3C_2T_x$ MXenes through tailoring the microstructure and surface functionalities. (a) Schematic illustration of high energy barrier and weak lithium adsorption of $Ti_3C_2T_x$ MXenes with a high ratio of fluorine and hydroxyl functionalized groups. (b) Schematic illustration of low energy barrier and strong lithium adsorption of $Ti_3C_2T_x$ MXenes with a low ratio of fluorine and hydroxyl functionalized groups. (c) Schematic illustration of preparing functionalized $Ti_3C_2T_x$ MXenes and tailoring surface functionalities of $Ti_3C_2T_x$ MXenes. (d) Representative SEM images of $Ti_3C_2T_x$ MXene sheets. The ripples of $Ti_3C_2T_x$ MXene sheets imply their intrinsic flexibility. (e) AFM image of MXene sheets, indicating the thickness of $Ti_3C_2T_x$ monolayer is about 2.5 nm. (f) Cross-sectional SEM images of $Ti_3C_2T_x$ MXene films.

capacitance could also be amazingly increased by nearly 10 times by eliminating the surface groups on Ti_2CT_x MXenes.[22] Although elimination of heteroatoms improves the electrical conductivity and promotes Li storage capacities, the presence of surface functionalities repulsing each other is considered helpful for avoiding the severe restack of 2D MXenes, which facilitates rapid ion transfer. On the other hand, the effect of the surface chemistry evolution on the electronic structure also needs to be further addressed. Till now, it is still an open question why surface chemistry and electronic structure are so influential to the Li storage capability.

2. METHODS

2.1. DFT Computations. All calculations were performed using the Vienna ab initio simulation package (VASP) based on density functional theory (DFT). The Perdew−Burke−Ernzerhof exchange function of the generalized gradient approximation was chosen for the calculations, and the projector-augmented wave pseudopotentials were employed for all ion−electron interactions. Considering both the convergence tests and the computational efficiency, an energy cutoff of 480 eV was chosen for the $Ti_3C_2T_x$ monolayer to ensure that the total energies were converged within 1×10^{-6} eV per atom. For geometry optimization, Brillouin zone sampling of the $Ti_3C_2T_x$ monolayer units was carried out with $9 \times 9 \times 1$ meshes using the Monkhorst−Pack method. Meanwhile, the denser mesh of $15 \times 15 \times 1$ was used for computing the density of states (DOS) of the $Ti_3C_2T_x$ monolayer units. The DFT-D2 method was introduced to consider the van der Waals effect on the atomic interactions of MXenes. For eliminating the interactions between the monolayer and adjacent conformations, a vacuum region of 20 Å was applied in the direction perpendicular to the $Ti_3C_2T_x$ supercells. To investigate Li-ion diffusion barriers and minimum energy paths, the climbing-image nudged elastic band method implemented in VASP was applied.

2.2. Preparation of Heteroatom-Controllable $Ti_3C_2T_x$ MXene Films. The preparation of Ti_3AlC_2 powders was

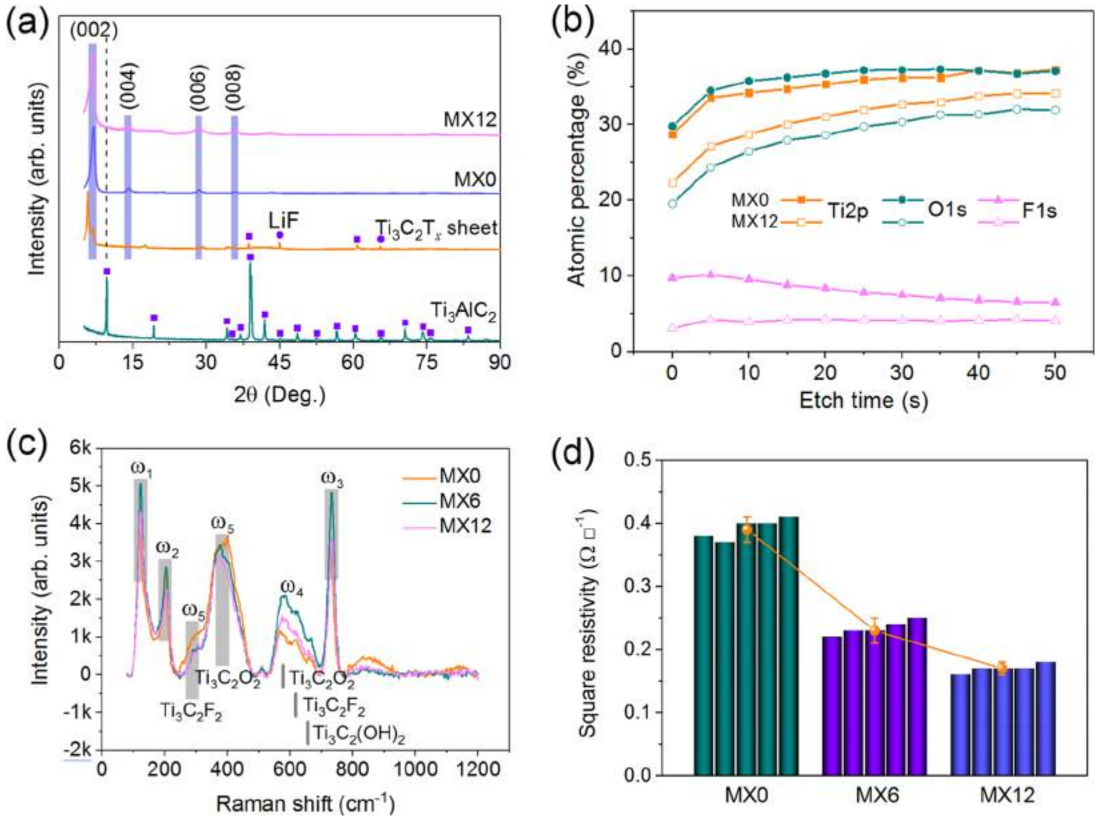

Figure 2. Compositions and electrical conductivity of freestanding $Ti_3C_2T_x$ MXene films. (a) XRD patterns of $Ti_3C_2T_x$ MXene films with and without annealing. The precursor Ti_3AlC_2 and the $Ti_3C_2T_x$ powder are also given for comparison. (b) The atomic percentage depends on the etch time of the MXene films determined by XPS depth profiling. (c) Representative Raman spectra of $Ti_3C_2T_x$ MXene films. (d) The sheet resistivity of different $Ti_3C_2T_x$ films determined by the four-probe method.

reported elsewhere.[23] Briefly, titanium (99%, GRINM, China), aluminum (99%, GRINM, China), and carbon black (99%, GRINM, China) powders in a 3:1.2:1.9 molar ratio were mixed, ball-milled, molded, and finally sintered at 1500 °C in a flowing argon atmosphere through a spark plasma sintering method (FCT, Rauenstein, Germany). The exfoliation and delamination of Ti_3AlC_2 powders to obtain the $Ti_3C_2T_x$ MXene colloidal solution were previously reported by our work.[24] The freestanding flexible $Ti_3C_2T_x$ MXene films with desired thickness underwent vacuum-assisted filtration by control of the volume and concentration of the colloidal aqueous solutions. Finally, for tailoring surface functional groups and the electronic structure, $Ti_3C_2T_x$ MXene films were carefully annealed by adjusting the annealing temperature from 200 to 600 °C, the annealing time from 0 to 12 h, the annealing atmosphere, and the heating rates. The samples were named as MX0, MX6, and MX12 corresponding to the annealing time.

2.3. Characterizations. X-ray diffraction (XRD) patterns were obtained with a PANlytical X'Pert Powder diffractometer. Scanning electron microscopy (SEM) and X-ray energy dispersive spectroscopy (EDX, JSM-7800F Prime) were used for morphology detection of pristine and annealed films and conduct elemental mapping analysis. Atomic force microscopy (AFM) was performed on an MFP-3D Infinity Asylum Research AFM. Water-stable colloidal solution dropped onto ultra-thin carbon-supported Cu mesh was investigated by TEM and HRTEM (JEOL JEM-2100), with an accelerating voltage of 200 kV. X-ray photoelectron spectroscopy (XPS) depth profile was recorded with a Thermo Scientific ESCALAB 250Xi spectrometer with chamber pressure maintained in the $10^{-6}-10^{-7}$ Pa range. Raman spectra of the samples were obtained from a RM2000 microscopic confocal Raman spectrometer with a 514 nm Ar-ion laser beam. The film resistances of heteroatom-controllable $Ti_3C_2T_x$ MXene films were measured using a four-probe technique (RTS8, China). The mass of the MXene electrodes was determined by a precision electronic balance (ME36S, Sartouris) with an accuracy of 1 μg.

2.4. Electrochemical Measurements. The cyclic voltammetry (CV) and electrochemical impedance spectroscopy (EIS) were conducted with a CHI 660E electrochemical workstation (Chenhua, Shanghai, China). The galvanostatic charge/discharge (GCD) and cycling stability measurement were carried out on an Arbin MSTAT4 multichannel galvanostat/potentiostat instrument (Arbin). The measured cells named MB0, MB6, and MB12 were used with MX0, MX6, and MX12 as the anodes, respectively.

3. RESULTS AND DISCUSSION

In this work, we realize extraordinary Li storage capabilities through lowering the diffusion energy barriers and boosting Li adsorption energy, in combined experimental and theoretical investigations, for $Ti_3C_2T_x$ films used as the LIB anodes (Figure 1a,b). Freestanding flexible $Ti_3C_2T_x$ films (the detailed information for samples and corresponding LIBs is given in Table S1) exhibit a high ratio of carboxyl, whereas a low ratio of hydroxyl and fluorine groups is observed after heat treatment in N_2/H_2 atmosphere with prolonged reaction

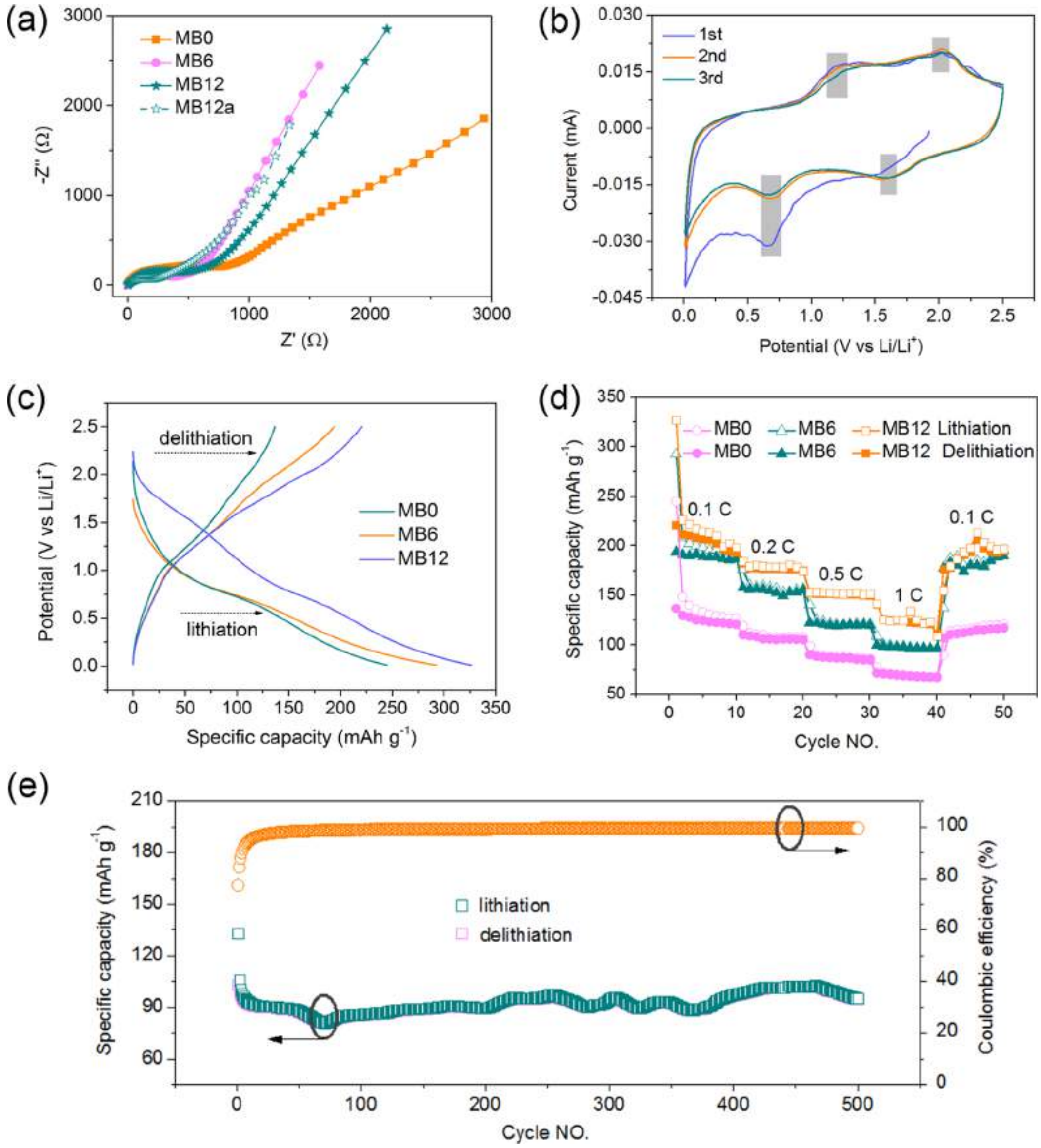

Figure 3. Lithium-ion batteries (LIBs) based on the substrate-free highly conductive $Ti_3C_2T_x$ MXene films. (a) The EIS plots at open-circuit potential. The EIS curve of MB12a after GCD cycling is also shown for comparison. (b) Typical CV curves of Li^+ insertion and deinsertion into functionalized highly conductive $Ti_3C_2T_x$ along with both oxidation and reduction processes. The first three cycles at 0.1 mV s^{-1} are shown. (c) Representative first-cycle GCD curves at a current rate of 0.1 C. (d) Gravimetric capacity at different current densities as a function of the charge rate for various $Ti_3C_2T_x$ MXene films. (e) Long-term cyclic stability and Coulombic efficiency of $Ti_3C_2T_x$ MXene-based LIBs after 500 cycles at a current rate of 1 C.

time (Figure 1c); the sheet resistance of $Ti_3C_2T_x$ films decreases by 1.4 times after carefully tailoring the surface chemistry. Consequently, the freestanding flexible $Ti_3C_2T_x$ films with high conductivity can be directly used as the substrate- and binder-free LIB anodes. Dramatically, the $Ti_3C_2T_x$ MXene films show reversible capacities of >200 mAh g^{-1} for lithium-ion batteries at a current density of 0.1 C (1 C = 320 mAh g^{-1}), which is the highest reported so far for pure $Ti_3C_2T_x$ MXene materials, including other Ti-based MXenes.[19,25,28] Our DFT computations reveal that this extraordinary Li storage capability is related to low diffusion energy barriers and strong Li adsorption. Through tailoring surface chemistry and electronic structure to boost Li-ion storage capability, the present work guides further studies on designing high-performance MXene-based materials for practical applications.

The representative scanning electron microscopy (SEM) image of $Ti_3C_2T_x$ MXene platelets is shown in Figure 1d, in which the MXene platelets show flexibility as demonstrated by self-generated corrugations of the platelets. In fact, the vacuum-filtrated $Ti_3C_2T_x$ MXene films possess good mechanical flexibility and maintain this peculiarity for annealed films (SI, Figures S1−S3). According to noncontact atomic force microscopy (AFM) images (Figure 1e), the MXene membranes are partially curved at the edges, again indicating the intrinsic flexibility. The step height at the edge of the flake is about ∼2.5 nm, as marked in Figure 1e and Figure S4 (SI). According to the high-resolution transmission electron microscopy (HRTEM) characterization (SI, Figure S5), the interlay spacing of $Ti_3C_2T_x$ MXene sheets is around 2.0 nm. The enlarged thickness determined by AFM measurement could be attributed to a number of factors that include AFM

DOI: 10.1021/acs.jpcc.8b11255
J. Phys. Chem. C 2019, 123, 2792−2800

tip−surface interactions, the interaction with an extrinsic substrate, and presence of trapped interfacial water molecules, among others.[29] The thickness of the pristine $Ti_3C_2T_x$ films with ordered layer stacking is approximately ∼900 nm, as determined by the cross-sectional SEM image (Figure 1f), and the thickness could be tailored as reported by our previous work.[24] These morphological characterizations clearly demonstrate that $Ti_3C_2T_x$ MXene platelets with large interlayer spacing and intrinsic flexibility can be assembled into freestanding flexible layered $Ti_3C_2T_x$ MXene films. The phase characteristics of pristine and annealed $Ti_3C_2T_x$ MXene films are determined by X-ray diffraction (XRD), as shown in Figure 2a. The precursors Ti_3AlC_2 with ternary-layered structure (SI, Figure S6) transform into 2D MXenes. Four typical diffraction peaks can be ascribed to the (002), (004), (006), and (008) planes of $Ti_3C_2T_x$ MXenes. In XRD pattern, any impurities of TiO_2 reflection in MX12 are not detected, implying that the heat treatment in N_2/H_2 atmosphere at 400 °C does not affect the thermal stability of $Ti_3C_2T_x$ MXenes. However, there is an apparent 2θ increment for (002) diffraction peak of MX12 in comparison to that of MX0, indicating a little bit of restack. This restack may be ascribed to the elimination of surface terminations and trapped water molecules on and between the layers.

For analyzing the annealing treatment effect on the surface chemistry, we performed XPS depth profiling for $Ti_3C_2T_x$ MXene films. The atomic percentages of Ti, C, O, and F dependencies on etch time are plotted in Figure 2b. As shown in Figure 2b, the dominant compositions of the samples are Ti, C, O, and F with very few traces of Al (SI, Figures S7 and S8). These results are similar with the EDX mapping results (SI, Figure S9). As expected, the F ratio is sharply decreased from 8.1 atom % for MX12 to 4.1 atom % for MX0 after the annealing treatment. In contrast, both the Ti and O concentrations increase with prolonging sputter time. XPS high-resolution spectra of C, O, and Ti further imply that the O concentrations are higher for the annealed samples than those for the pristine one (SI, Figure S10). In addition, the XPS of F element shows an invariant peak position on varying the thickness of the films (SI, Figure S11). From the results shown above, it can be concluded that the annealed samples are mainly composed of Ti_3C_2 MXene with higher O and lower F&OH terminations than those of pristine samples.

Raman spectroscopy, very sensitive to tiny changes in crystal structures, further proves the evolution of surface-functionalized groups. The bands at around 122, 207, 386, 585, 732, and 840 cm^{-1} are indicative of $Ti_3C_2T_x$ MXenes (Figure 2c).[30,31] After annealing treatment and on prolonging annealing time, the Raman bands at 386 and 585 cm^{-1} shift to the lower wavenumbers, demonstrating that the ratio of $Ti_3C_2O_2$ increases whereas that of $Ti_3C_2F_2$ and $Ti_3C_2(OH)_2$ decreases (Figure 2c). Our deconvolution of the band at ∼585 cm^{-1} further (SI, Figure S12) demonstrates that the ratio of $Ti_3C_2O_2$ for MX6 and MX12 increases by 15 and 20% in comparison to that of MX0. In addition, the Raman active modes at around 386 and 585 cm^{-1} show several apparent humps, reflecting the fact that the terminal groups are actually heterogeneous,[30] which coincides with our XPS results.

Materials with large electrical conductivity are typically needed to obtain high-rate LIB electrodes. Figure 2d presents the electrical conductivity of pristine and annealed $Ti_2C_3T_x$ MXenes. A higher electrical conductivity in MX12 is observed compared to that in MX0 and MX6. MX12 $Ti_3C_2T_x$ films showed the lowest sheet resistance among the studied samples, reaching 0.17 ± 0.01 $\Omega\ \square^{-1}$. By contrast, MX0 and MX6 exhibit higher sheet resistance values of 0.40 ± 0.02 and 0.23 ± 0.02 $\Omega\ \square^{-1}$, respectively. The increased electrical conductivity may be attributed to the elimination of F element and some structural defects after annealing treatment. In short, after carefully controlling the parameters of annealing treatment, the annealed $Ti_3C_2T_x$ MXenes show lower contents of F&OH terminations and higher electrical conductivity in comparison with the pristine samples.

Since the harmful terminations are efficiently eliminated and the electrical conductivity is enhanced without incorporating the impurities, we anticipate that the Li storage of annealed $Ti_3C_2T_x$ MXene films would be improved. The electrochemical measurements were carried out to observe the feasibility of using flexible substrate- and binder-free $Ti_3C_2T_x$ MXene films in LIBs. Figure 3a shows electrochemical impedance spectra (EIS) of $Ti_3C_2T_x$ anode in a 1 M $LiPF_6$/ethylene carbonate−dimethyl carbonate electrolyte at the open-circuit voltage. As expected, the MB6 and MB12 using MX6 and MX12 as the anodes, respectively, show much more lower diffusion resistance than that of MB0 with MX0 as the anode. After 50 cycles from 0.1 to 1 C, the internal resistance and Warburg impedance of MB12a further decline due to the formation of a solid electrolyte interface (SEI), which promotes ionic migration.[32] Figure 3b shows cyclic voltammetry (CV) curves of $Ti_3C_2T_x$ anodes using a 0.1 mV s^{-1} scan rate. The first cathodic scan exhibits an irreversible current at a voltage of ∼0.72 V (vs Li/Li^+) due to the formation of an SEI layer.[33] This behavior commonly appears in 2D materials, like graphene, MoS_2, and other MXenes.[34−37] Another phenomenon is that all subsequent CV cycles exhibit stable quasirectangular CVs, which is different from the commercial LIB anodes, like graphite and lithium titanate. The two well-defined redox peaks in the CVs of MB12 correspond to the Li^+ insertion−deinsertion reaction as follows

$$y\mathrm{Li}^+ + \mathrm{Ti_3C_2T}_x + y\mathrm{e}^- \leftrightarrow \mathrm{Ti_3C_2T}_x\mathrm{Li}_y$$

Figure 3c shows the first galvanostatic charge/discharge (GCD) curves measured in the voltage range of 0.01−2.5 V (vs Li/Li^+) at a current rate of 0.1 C. The first charge curve shows a capacitive slope but with a little smaller capacity of 221 mAh g^{-1}, resulting in a low Coulombic efficiency of 68% for the first cycle. The large irreversibility of 32% and low Coulombic efficiency of $Ti_3C_2T_x$ at the initial charge/discharge cycle are similar to the previously reported results for $Ti_3C_2T_x$ and Ti_2CT_x.[38−40] The irreversible capacity loss is most likely caused by side reactions, such as SEI formation and electrolyte decomposition. The flexible substrate- and binder-free $Ti_3C_2T_x$ exhibits good rate capability, as shown in Figure 3d. When cycled at a high rate of 1 C, still 124 mAh g^{-1} can remain, that is 56% initial retention at 0.1 C. The reversible capacity of MB12 reaches up to ∼200 mAh g^{-1}, which is higher than that of other pure Ti-based MXenes[19,25−27] but lower than that of delaminated $Ti_3C_2T_x$ and some composites.[34,41,42] Remarkably, an exceptionally long lifetime of 500 cycles is achieved with a stable capacity of ∼100 mAh g^{-1} when cycled at 1 C (Figure 3e). The good cycle stability and high-rate capability of $Ti_3C_2T_x$ indicate this material as a potential candidate for energy storage applications.

For more details about effect of surface chemistry and electronic structure on Li-ion storage capability of the $Ti_3C_2T_x$

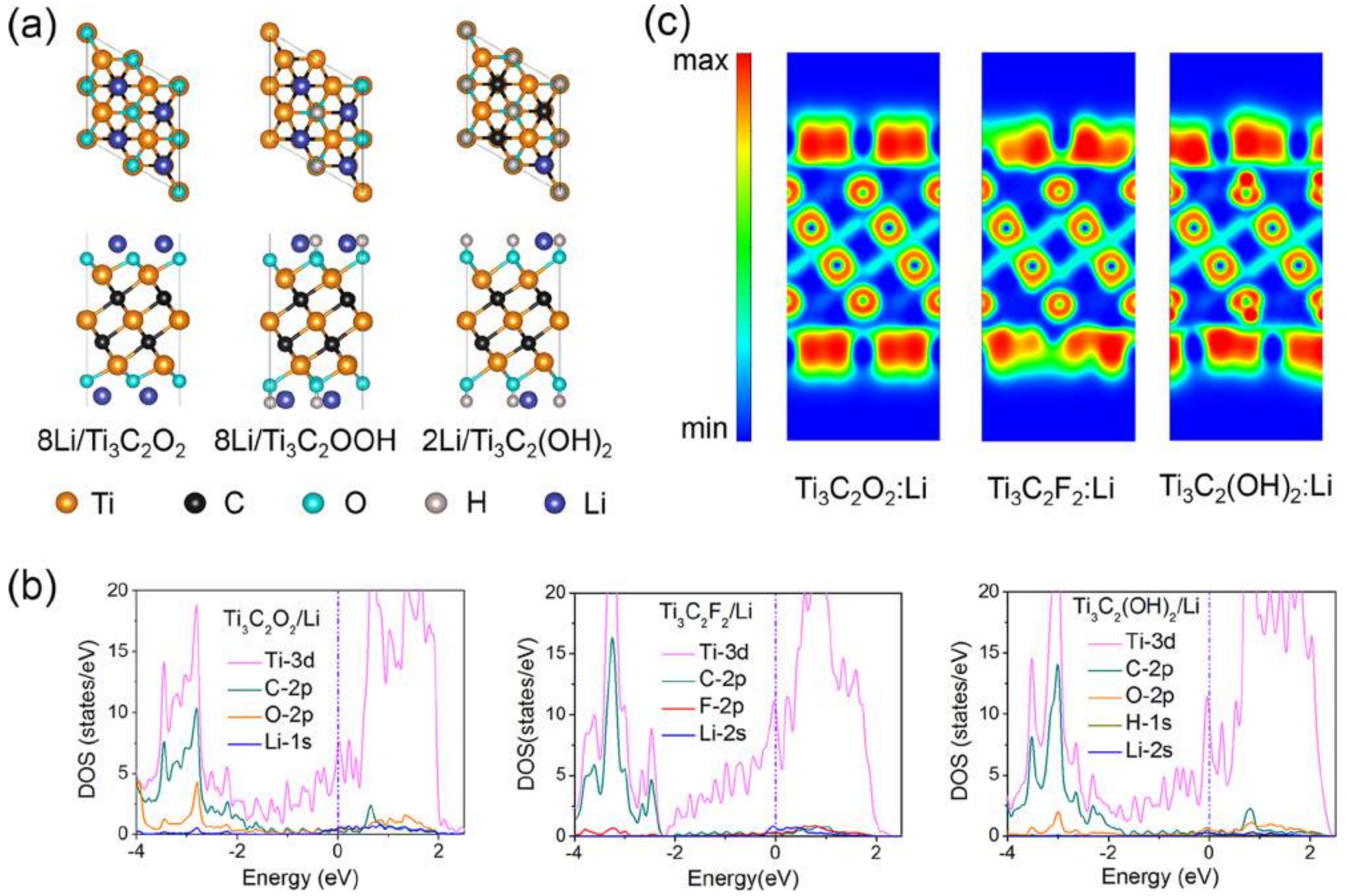

Figure 4. DFT calculations of the geometry and electronic structures for Li-decorated Ti$_3$C$_2$T$_x$ supercells. (a) Top (upper row) and side (lower row) views showing the different functionalized Ti$_3$C$_2$T$_x$ structures (2 × 2 supercells) with Li atoms adsorbed. (b) Orbitally resolved densities of states of Ti$_3$C$_2$O$_2$, Ti$_3$C$_2$OOH, and Ti$_3$C$_2$(OH)$_2$ with maximum Li atoms adsorbed. The Fermi level is set to 0 eV, which is marked with a purple dotted line. (c) Valence ELF of (110) sections of lithiated Ti$_3$C$_2$O$_2$, Ti$_3$C$_2$F$_2$, and Ti$_3$C$_2$(OH)$_2$ supercells.

MXenes, we performed DFT calculations with Ti$_3$C$_2$ monolayer functionalized by O, OH, and F groups. Here, we mainly studied seven different Ti$_3$C$_2$T$_x$ MXenes labeled Ti$_3$C$_2$O$_2$, Ti$_3$C$_2$F$_2$, Ti$_3$C$_2$(OH)$_2$, Ti$_3$C$_2$O$_{1.75}$F$_{0.25}$, Ti$_3$C$_2$O$_{1.75}$(OH)$_{0.25}$, Ti$_3$C$_2$O(OH), and Ti$_3$C$_2$O$_{0.75}$F$_{0.25}$(OH). After full optimization, it is found that the O, OH, and F atoms all prefer to locate at the hollow sites among the three neighboring C atoms (Figure 4a). The lattice parameters and the bond lengths of Ti−C, Ti−O, Ti−F, C−O, and C−F in the ground state are collected in Table S2, in good agreement with the previous studies.[43] Due to O, F, and OH functionalization, the length of Ti−C is elongated compared to that in the bare Ti$_3$C$_2$. The bond length of O/F and Ti and O/F and C in Ti$_3$C$_2$O$_2$ and Ti$_3$C$_2$F$_2$ is shorter than that of Ti−O and C−O in Ti$_3$C$_2$(OH)$_2$ because of the different oxidation states of the anionic elements, which indicates stronger interaction between O/F and Ti$_3$C$_2$.

To explore the Li storage capability, various Li coverage rates of Li atoms adsorbed on the Ti$_2$C$_3$T$_x$ with a 2 × 2 supercell are studied. Specifically, as many as 8 Li atoms can be adsorbed for Ti$_3$C$_2$O$_2$, which is the highest concentration of Li atoms adsorbed on all of these Ti$_2$C$_3$T$_x$. The maximum number of Li atoms that can be adsorbed decreases when some of the O of the Ti$_3$C$_2$O$_2$ are replaced by F or OH. For example, only 6 Li atoms can be adsorbed on Ti$_3$C$_2$O$_{0.75}$F$_{0.25}$(OH), 4 Li on Ti$_3$C$_2$F$_{0.25}$(OH)$_{1.75}$, and Ti$_3$C$_2$F$_2$ and 2 Li on Ti$_3$C$_2$(OH)$_2$, respectively. This reveals that dominant O termination with less F&OH groups is helpful for Li-ion storage capacity. To assess the stabilities of lithiated Ti$_2$C$_3$T$_x$, the adsorption energy was calculated with: $E_{ad} = (E_{Li\text{-}MX} - E_{MX} - nE_{Li})/n$, where $E_{Li\text{-}MX}$ is the total energy of a lithiated monolayer, E_{MX} denotes the total energy of bare MXene monolayer, E_{Li} is the chemical potential of Li atom, and n presents the number of adsorbed Li atoms. The adsorption energies are summarized in Table S2 where lower E_{ad} values mean stronger binding of Li to the Ti$_2$C$_3$T$_x$ surfaces. For Ti$_3$C$_2$O$_2$, Ti$_3$C$_2$F$_2$, and Ti$_3$C$_2$(OH)$_2$, the adsorption energies are −1.581, −0.222, and −0.053 eV per Li atom, respectively. For other compounds with mixed O, F, and OH terminations, the adsorption energies are between −1.58 and −0.053 eV per Li atom, suggesting the adsorption strength of Li atoms highly depends on the terminations and the order from strong to weak is O > F > OH. These theoretical results unambiguously imply that the annealed Ti$_2$C$_3$T$_x$ MXenes possess high Li-ion adsorption energy after efficiently eliminating the partial of F&OH terminations and hence can deliver high Li-ion storage capacity.

Next, we studied the diffusion barriers for Li atoms on the surfaces of Ti$_2$C$_3$T$_x$ monolayers. Except for the Ti$_3$C$_2$ MXene fully terminated by O with a 3 × 3 supercell, Ti$_{27}$C$_{18}$O$_{18}$, two other configurations Ti$_{27}$C$_{18}$O$_{17}$F and Ti$_{27}$C$_{18}$O$_{17}$(OH) are studied for the influence of a few F and OH groups on the Li diffusion due to the small amounts of F and OH components observed in our experiments. Among different diffusion pathways, the one that Li ion prefers to migrate on is C →

Ti → C. The energy barriers for $Ti_{27}C_{18}O_{18}$, $Ti_{27}C_{18}O_{17}F$, and $Ti_{27}C_{18}O_{17}(OH)$ are 0.36, 0.34, and 0.43 eV, respectively, which indicates that a few of F atoms influence little the Li diffusion at O-terminated Ti_3C_2 MXene, whereas OH group draws back a lot. In Figure 4b and Figure S13, we show the performing projected density of states (PDOS) of the lithiated $Ti_2C_3T_x$ monolayers. Similar to Ti_3C_2, the lithiated $Ti_3C_2O_2$, $Ti_3C_2(OH)_2$, and $Ti_3C_2F_2$ monolayers are intrinsically metallic, with a large number of electronic states near the Fermi level.[44,45] Besides, there is much more hybridization between the O p or F p and Li s states than that between O p, H s, and Li s, which supports the results of Li adsorption energy shown above.

Considering that the first Li layer cannot be utilized completely and the extra Li layer can be adsorbed, we introduce one more Li layer (second Li layer) on the first Li layer-$Ti_3C_2T_x$. The adsorption energy E_{ad} of the second Li layer is used to check the stability of the structure: $E_{ad} = (E_{Li\text{-}Li\text{-}M} - E_{Li\text{-}M} - mE_{Li})/m$. The adsorption energies of the second Li layer are about ~1.58 to ~1.68 eV, shown in Table S3. Compared with the bcc Li cohesive energy of −1.701 eV/atom in our calculations, apparently the E_{ad} values are larger, which indicates the possibility of the second Li layer being adsorbed on the first Li layer-$Ti_3C_2T_x$. As shown in Table S3, the number of Li atoms that can be adsorbed in the second Li layer decreases as a certain amount of O groups is substituted by F&OH groups. For example, 8 Li atoms can be adsorbed in the extra layer for $Ti_3C_2O_2$, $Ti_3C_2(OH)_2$, $Ti_3C_2F_2$, $Ti_3C_2O_{1.75}F_{0.25}$, and $Ti_3C_2O_{1.75}(OH)_{0.25}$, whereas for $Ti_3C_2O(OH)$ and $Ti_3C_2O_{0.75}F_{0.25}(OH)$, only 2 Li atoms can be adsorbed. In Figure 4c, we show the valence electron localization function (ELF) of the lithiated $Ti_3C_2O_2$, $Ti_3C_2F_2$, and $Ti_3C_2(OH)_2$ with two Li layers. For comparison, the ELF of the lithiated MXenes with mixed functionalized groups is also shown (SI, Figure S14). Apparently, electron transfer occurs between the second Li layer and the first Li layer-$Ti_2C_3T_x$. The amount of charge transfer was estimated quantitatively by the Bader charge analysis. It shows that the extra Li layer acts as an electron donor as about 0.77 and 0.54*e* are transferred to the first Li layer for $Ti_3C_2F_2$ and $Ti_3C_2(OH)_2$, respectively, whereas for $Ti_3C_2O_2$, the extra Li layer acts as an electron acceptor with about 0.16*e* transferred from the first Li layer. This may be due to the larger amount of Li atoms in the first Li layer of $Ti_3C_2O_2$ than that in the first Li layers of $Ti_3C_2F_2$ and $Ti_3C_2(OH)_2$.

In view of the computation results shown above, we can see that $Ti_3C_2T_x$ with higher O and fewer F&OH terminations shows higher Li content considering two Li layers, stronger adsorption strength for Li adatoms among the $Ti_2C_3T_x$, and a low energy barrier for Li diffusion. For O termination-dominated Ti_3C_2, a small number of F&OH groups have less influence whereas more F&OH groups result in weaker adsorption strength, less Li content, and a higher diffusion barrier. In good agreement with our experiment, the O-dominated MX6 and MX12 exhibit superior Li-ion storage capability.

4. CONCLUSIONS

In conclusion, we have systematically investigated the surface chemistry and electronic structure effects on Li-ion storage capabilities of functionalized MXenes using a combination of experimental and theoretical approaches. We confirm that careful annealing treatment is efficient to tailor the surface-functionalized groups without incorporating any impurities. The surface heteroatoms' controllability in turn affects the electronic structure of MXenes. A high reversible Li-ion capacity and good rate capability for freestanding $Ti_3C_2T_x$ MXene films with low contents of F&OH terminations along with enhanced electrical conductivity are achieved. Calculations of the Li-ion storage capacity of terminated MXenes predict sufficient capacity and rate-capability attributes from lower Li diffusion barriers and stronger Li adsorption. Our combined experimental and theoretical findings disclosing the boost of Li storage capabilities via tailoring surface chemistry and electronic structure of 2D MXenes pave the way for designing high-performance energy storage devices as well as catalytic, optoelectronic, and thermoelectric devices based on other 2D materials.

■ ASSOCIATED CONTENT

Ⓢ Supporting Information

The Supporting Information is available free of charge on the ACS Publications website at DOI: 10.1021/acs.jpcc.8b11255.

> Preparation of MXene colloidal solution and films, morphological characterizations of MXene films; compositions of both pristine and annealed MXene films; DOS and ELF of MXene supercells; detailed samples information; lattice parameters; adsorption energy of different MXene systems (PDF)

■ AUTHOR INFORMATION

Corresponding Authors

*E-mail: csguo@swjtu.edu.cn (C.G.).
*E-mail: wqyang@swjtu.edu.cn (W.Y.).

ORCID

Chunsheng Guo: 0000-0002-2037-1533
Weiqing Yang: 0000-0001-8828-9862

Author Contributions

⊥H.Z. and X.X. contributed equally to this work.

Author Contributions

H.T.Z. and W.Q.Y. proposed and designed the project, C.S.G. and X.J.X. carried out theoretical calculations, H.T.Z., H.L., and H.C.H performed the experiments, H.T.Z., N.J.C, Y.T.X, and W.L.D. performed characterizations, and H.T.Z., H.L., and H.C.H. analyzed data. The manuscript was written through contributions of all authors. All authors have given approval to the final version of the manuscript.

Notes

The authors declare no competing financial interest.

■ ACKNOWLEDGMENTS

We are thankful to the Analytical and Testing Center of Southwest Jiaotong University for supporting the SEM measurements. This work is supported by the National Natural Science Foundation of China (No. 51602265) and Special Funding of China Postdoctoral Science Foundation (2018T110992).

■ REFERENCES

(1) Anasori, B.; Lukatskaya, M. R.; Gogotsi, Y. 2D metal carbides and nitrides (MXenes) for energy storage. *Nat. Rev. Mater.* **2017**, *2*, No. 16098.

(2) El-Kady, M. F.; Shao, Y. L.; Kaner, R. B. Graphene for batteries, supercapacitors and beyond. *Nat. Rev. Mater.* **2016**, *1*, No. 16033.

(3) Azadmanjiri, J.; Wang, J.; Berndt, C. C.; Yu, A. M. 2D layered organic-inorganic heterostructures for clean energy applications. *J. Mater. Chem. A* **2018**, *6*, 3824−3849.

(4) Solís-Fernández, P.; Bissett, M.; Ago, H. Synthesis, structure and applications of graphene-based 2D heterostructures. *Chem. Soc. Rev.* **2017**, *46*, 4572−4613.

(5) Wang, T. Y.; Chen, S. Q.; Pang, H.; Xue, H. G.; Yu, Y. MoS_2-based nanocomposites for electrochemical energy storage. *Adv. Sci.* **2017**, *4*, No. 1600289.

(6) Naguib, M.; Kurtoglu, M.; Presser, V.; Lu, J.; Niu, J. J.; Heon, M.; Hultman, L.; Gogotsi, Y.; Barsoum, M. W. Two-dimensional nanocrystals produced by exfoliation of Ti_3AlC_2. *Adv. Mater.* **2011**, *23*, 4248−4253.

(7) Naguib, M.; Mochalin, V. N.; Barsoum, M. W.; Gogotsi, Y. 25th anniversary article: MXenes: a new family of two-dimensional materials. *Adv. Mater.* **2014**, *26*, 992−1005.

(8) Okubo, M.; Sugahara, A.; Kajiyama, S.; Yamada, A. MXene as a charge storage host. *Acc. Chem. Res.* **2018**, *51*, 591−599.

(9) Xiong, D. B.; Li, X. F.; Bai, Z. M.; Lu, S. G. Recent advances in layered $Ti_3C_2T_x$ MXene for electrochemical energy storage. *Small* **2018**, *14*, No. 1703419.

(10) Tang, Q.; Zhou, Z.; Shen, P. Are MXenes promising anode materials for Li ion batteries? Computational studies on electronic properties and Li storage capability of Ti_3C_2 and $Ti_3C_2X_2$ (X = F, OH) monolayer. *J. Am. Chem. Soc.* **2012**, *134*, 16909−16.

(11) Persson, K.; Hinuma, Y.; Meng, Y. S.; Van der Ven, A.; Ceder, G. Thermodynamic and kinetic properties of the Li-graphite system from first-principles calculations. *Phys. Rev. B* **2010**, *82*, No. 125416.

(12) Ziebarth, B.; Klinsmann, M.; Eckl, T.; Elsasser, C. Lithium diffusion in the spinel phase $Li_4Ti_5O_{12}$ and in the rocksalt phase $Li_7Ti_5O_{12}$ of lithium titanate from first principles. *Phys. Rev. B* **2014**, *89*, No. 174301.

(13) Xie, Y.; Naguib, M.; Mochalin, V. N.; Barsoum, M. W.; Gogotsi, Y.; Yu, X.; Nam, K. W.; Yang, X. Q.; Kolesnik, Al.; Kent, P. R. C. Role of surface structure on Li-ion energy storage capacity of two-dimensional transition-metal carbides. *J. Am. Chem. Soc.* **2014**, *136*, 6385−94.

(14) Ashton, M.; Hennig, R. G.; Sinnott, S. B. Computational characterization of lightweight multilayer MXene Li-ion battery anodes. *Appl. Phys. Lett.* **2016**, *108*, No. 023901.

(15) Lv, X.; Wei, W.; Sun, Q.; Yu, L.; Huang, B.; Dai, Y. Sc_2C as a Promising anode material with high mobility and capacity: a first-principles study. *ChemPhysChem* **2017**, *18*, 1627−1634.

(16) Xu, Z.; Lv, X.; Chen, J.; Jiang, L.; Lai, Y.; Li, J. DFT investigation of capacious, ultrafast and highly conductive hexagonal Cr_2C and V_2C monolayers as anode materials for high-performance lithium-ion batteries. *Phys. Chem. Chem. Phys.* **2017**, *19*, 7807−7819.

(17) Hope, M. A.; Forse, A. C.; Griffith, K. J.; Lukatskaya, M. R.; Ghidiu, M.; Gogotsi, Y.; Grey, C. P. NMR reveals the surface functionalisation of Ti_3C_2 MXene. *Phys. Chem. Chem. Phys.* **2016**, *18*, 5099−5102.

(18) Ashton, M. M.; Kiran, H.; Richard, G.; Sinnott, S. B. Predicted surface composition and thermodynamic stability of MXenes in solution. *J. Phys. Chem. C* **2016**, *120*, 3550−3556.

(19) Wang, X.; Shen, X.; Gao, Y.; Wang, Z.; Yu, R.; Chen, L. Atomic-scale recognition of surface structure and intercalation mechanism of Ti_3C_2X. *J. Am. Chem. Soc.* **2015**, *137*, 2715−21.

(20) Wang, H. W.; Naguib, M.; Page, K.; Gogotsi, Y.; et al. Resolving the Structure of $Ti_3C_2T_x$ MXenes through multilevel structural modeling of the atomic pair distribution function. *Chem. Mater.* **2015**, *28*, 349−359.

(21) Karlsson, L. H.; Birch, J.; Halim, J.; Barsoum, M. W.; Persson, P. O. Atomically resolved structural and chemical investigation of single MXene sheets. *Nano Lett.* **2015**, *15*, 4955−4960.

(22) Rakhi, R. B.; Ahmed, B.; Hedhili, M. N.; Anjum, D. H.; Alshareef, H. N. Effect of postetch annealing gas composition on the structural and electrochemical properties of Ti_2CT_x MXene electrodes for supercapacitor applications. *Chem. Mater.* **2015**, *27*, 5314−5323.

(23) Wang, C. X.; Yang, T. F.; Kong, S. Y.; Xiao, J. R.; Xue, J. M.; Wang, Q.; Hu, C. F.; Huang, Q.; Wang, Y. G. Effects of He irradiation on Ti_3AlC_2: Damage evolution and behavior of He bubbles. *J. Nucl. Mater.* **2013**, *440*, 606−611.

(24) Huang, H. C.; Su, H.; Zhang, H. T.; Xu, L. D.; Chu, X.; Hu, C. F.; Liu, H.; Chen, N. J.; Liu, F.; Y.; et al. Extraordinary areal and volumetric performance of flexible solid-state micro-supercapacitors based on highly conductive freestanding $Ti_3C_2T_x$ films. *Adv. Electron. Mater.* **2018**, *4*, No. 1800179.

(25) Naguib, M.; Come, J.; Dyatkin, B.; Presser, V.; Taberna, P. L.; Simon, P.; Barsoum, M. W.; Gogotsi, Y. MXene: a promising transition metal carbide anode for lithium-ion batteries. *Electrochem. Commun.* **2012**, *16*, 61−64.

(26) Sun, D. D.; Wang, M. S.; Li, Z. Y.; Fan, G. X.; Fan, L. Z.; Zhou, A. G. Two-dimensional Ti_3C_2 as anode material for Li-ion batteries. *Electrochem. Commun.* **2014**, *47*, 80−83.

(27) Kim, S. J.; Naguib, M.; Zhao, M. Q.; Zhang, C. F.; Jung, H. T.; Barsoum, M. W.; Gogotsi, Y. High mass loading, binder-free MXene anodes for high areal capacity Li-ion batteries. *Electrochim. Acta* **2015**, *163*, 246−251.

(28) Ren, C. E.; Zhao, M. Q.; Makaryan, T.; Halim, J.; Boota, M.; Kota, S.; Anasori, B.; Barsoum, M. W.; Gogotsi, Y. Porous Two-dimensional transition metal carbide (MXene) flakes for high-performance Li-ion storage. *ChemElectroChem* **2016**, *3*, 689−693.

(29) Lipatov, A.; Lu, H. D.; Alhabeb, M.; Anasori, B.; Gruverman, A.; Gogotsi, Y.; Sinitskii, A. Elastic properties of 2D $Ti_3C_2T_x$ MXene monolayers and bilayers. *Sci. Adv.* **2018**, *4*, No. eaat0491.

(30) Hu, T.; Wang, J. M.; Zhang, H.; Li, Z. J.; Hu, M. M.; Wang, X. H. Vibrational properties of Ti_3C_2 and $Ti_3C_2T_2$ (T = O, F, OH) monosheets by first-principles calculations: a comparative study. *Phys. Chem. Chem. Phys.* **2015**, *17*, 9997−10003.

(31) Hu, M. M.; Li, Z. J.; Hu, T.; Zhu, S. H.; Zhang, C.; Wang, X. H. High-capacitance mechanism for $Ti_3C_2T_x$ MXene by in situ electrochemical Raman spectroscopy investigation. *ACS Nano* **2016**, *10*, 11344−11350.

(32) Li, F. S.; Wu, Y. S.; Chou, J.; Winter, M.; Wu, N. L. A mechanically robust and highly ion-conductive polymer-blend coating for high-power and long-life lithium-ion battery anodes. *Adv. Mater.* **2015**, *27*, 130−137.

(33) Peled, E.; Menkin, S. Review-SEI: Past, present and future. *J. Electrochem. Soc.* **2017**, *164*, A1703−A1719.

(34) Yu, P.; Cao, G.; Yi, S.; Zhang, X.; Li, C.; Sun, X.; Wang, K.; Ma, Y. Binder-free 2D titanium carbide (MXene)/carbon nanotube composites for high-performance lithium-ion capacitors. *Nanoscale* **2018**, *10*, 5906−5913.

(35) Chen, Y. M.; Yu, X. Y.; Li, Z.; Paik, U.; Lou, X. W. Hierarchical MoS_2 tubular structures internally wired by carbon nanotubes as a highly stable anode material for lithium-ion batteries. *Sci. Adv.* **2016**, *2*, No. e1600021.

(36) Zhang, X. Y.; Hou, L. L.; Ciesielski, A.; Samori, P. 2D Materials Beyond Graphene for high-performance energy storage applications. *Adv. Energy Mater.* **2016**, *6*, No. 1600671.

(37) Su, H.; Zhang, H. T.; Liu, F. Y.; Chun, F. J.; Zhang, B. B.; Chu, X.; Huang, H. C.; Deng, W. L.; Gu, B. N.; et al. High power supercapacitors based on hierarchically porous sheet-like nanocarbons with ionic liquid electrolytes. *Chem. Eng. J.* **2017**, *322*, 73−81.

(38) Wang, Y. S.; Li, Y. Y.; Qiu, Z. P.; Wu, X. Z.; Zhou, P. F.; Zhou, T.; Zhao, J. P.; Miao, Z. C.; Zhou, J.; Zhuo, S. P. Fe_3O_4@Ti_3C_2 MXene hybrids with ultrahigh volumetric capacity as an anode material for lithium-ion batteries. *J. Mater. Chem. A* **2018**, *6*, 11189−11197.

(39) Luo, J. M.; Tao, X. Y.; Zhang, J.; Xia, Y.; Huang, H.; Zhang, L. Y.; Gan, Y. P.; Liang, C.; Zhang, W. K. Se^{4+} ion decorated highly conductive Ti_3C_2 MXene: promising lithium-ion anodes with enhanced volumetric capacity and cyclic performance. *ACS Nano* **2016**, *10*, 2491−2499.

(40) Li, L. F.; Wang, F.; Zhu, J. F.; Wu, W. L. The facile synthesis of layered Ti_2C MXene/carbon nanotube composite paper with

enhanced electrochemical properties. *Dalton Trans.* **2017**, *46*, 14880−14887.

(41) Zhu, J.; Schwingenschlögl, U. P and Si functionalized MXenes for metal-ion battery applications. *2D Mater.* **2017**, *4*, No. 025073.

(42) Wu, X.; Wang, Z.; Yu, M.; Xiu, L.; Qiu, J. Stabilizing the MXenes by carbon nanoplating for developing hierarchical nanohybrids with efficient lithium storage and hydrogen evolution capability. *Adv. Mater.* **2017**, *29*, No. 1607017.

(43) Xie, Y.; Kent, P. R. C. Hybrid density functional study of structural and electronic properties of functionalized $Ti_{n+1}X_n$(X = C, N) monolayers. *Phys. Rev. B* **2013**, *87*, No. 235441.

(44) Wu, F.; Luo, K.; Huang, C. X.; Wu, W. J.; Meng, P. W.; Liu, Y. F.; Kan, E. J. Theoretical understanding of magnetic and electronic structures of Ti_3C_2 monolayer and its derivatives. *Solid State Commun.* **2015**, *222*, 9−13.

(45) Anasori, B.; Shi, C. Y.; Moon, E. J.; Xie, Y.; Voigt, C. A.; Kent, P. R. C.; May, S. J.; Billinge, S. J. L.; Barsoum, M. W.; Gogotsi, Y. Control of electronic properties of 2D carbides (MXenes) by manipulating their transition metal layers. *Nanoscale Horiz.* **2016**, *1*, 227−234.